






RESEARCH ARTICLE | DECEMBER 26 2023

# Strained AlGaInAs on InP: Bandgap dependence on composition—Model benchmark and optimization

Marcin Zyskowski   ; Nick de Louw  ; Steven Kleijn  ; Francisco Javier Díaz Otero 



*J. Appl. Phys.* 134, 243103 (2023)

<https://doi.org/10.1063/5.0173760>

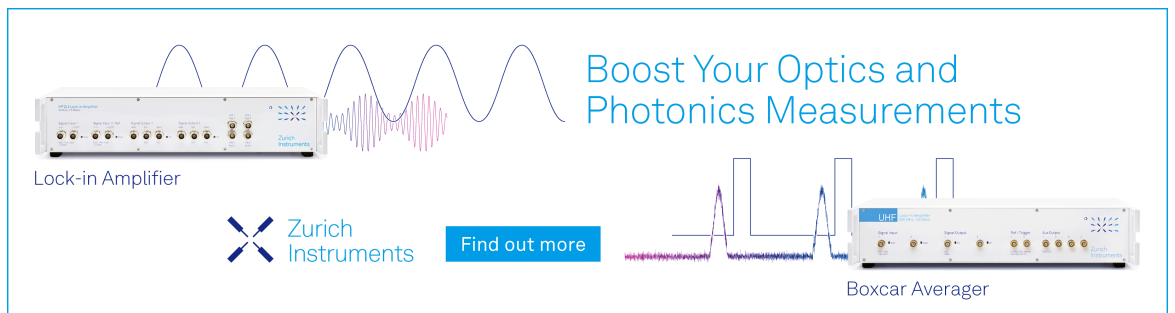


View  
Online



Export  
Citation

CrossMark



Boost Your Optics and Photonics Measurements

Lock-in Amplifier

Zurich Instruments

Find out more

Boxcar Averager

# Strained AlGaInAs on InP: Bandgap dependence on composition—Model benchmark and optimization

Cite as: J. Appl. Phys. **134**, 243103 (2023); doi: [10.1063/5.0173760](https://doi.org/10.1063/5.0173760)

Submitted: 24 August 2023 · Accepted: 5 December 2023 ·

Published Online: 26 December 2023



View Online



Export Citation



CrossMark

Marcin Zyskowski,<sup>1,2,a)</sup> Nick de Louw,<sup>1</sup> Steven Kleijn,<sup>1</sup> and Francisco Javier Díaz Otero<sup>2</sup>

## AFFILIATIONS

<sup>1</sup>SMART Photonics, High Tech Campus 37, 5656 AE Eindhoven, The Netherlands

<sup>2</sup>Universidade de Vigo, atlantTtic Research Centre, Maxwell s/n, University Campus, E36310 Vigo, Spain

<sup>a)</sup>Author to whom correspondence should be addressed: [zyskowskiscience@gmail.com](mailto:zyskowskiscience@gmail.com)

## ABSTRACT

Influence of chemical composition on the bandgap of AlGaInAs deposited on InP is often calculated using models for unstrained composition and then corrected for strain-induced bandgap energy changes using deformation potentials. This method relies on up to 25 coefficients, many of which are burdened with large uncertainty. In this paper, a large set of experimental data is used to verify the accuracy of existing approaches and to search for optimal deformation potentials. It is shown that the main source of inaccuracy is not the deformation potentials, but the unstrained bandgap formulas. Additionally, a novel model is proposed, yielding the highest accuracy on our dataset. For the first time, composition determination of a quaternary alloy on InP is reported using inductively coupled plasma-optical emission spectrometry, which is used as a benchmark for modeling.

© 2023 Author(s). All article content, except where otherwise noted, is licensed under a Creative Commons Attribution (CC BY) license (<http://creativecommons.org/licenses/by/4.0/>). <https://doi.org/10.1063/5.0173760>

## I. INTRODUCTION

AlGaInAs is an alloy of interest in semiconductor laser sources in 1300 and 1550 nm wavelength ranges of the optical spectrum, owing to the wide range of bandgaps and strains that can be achieved by varying its composition when deposited on InP.<sup>1,2</sup> To enable applications of AlGaInAs, one must accurately predict the bandgap of the epitaxially deposited alloy, based on its chemical composition. Particularly, the bandgap of strained compositions is of interest, as commercial diode lasers make use of strained layers of AlGaInAs to achieve the highest performance. In this paper, we present the use of aqueous elemental analysis for the determination of alloy composition and we suggest a new empirical model that determines the alloy's bandgap more accurately than the existing methods. We have found that while the existing methods are useful to determine which composition is required to obtain a desired bandgap, there is merit in optimizing the model further. Our empirical model significantly reduces the offset between predicted and measured bandgaps, which allows to grow complex layer stacks in fewer iterations.

In order to achieve a sound correlation between composition and bandgap, the chemical composition of AlGaInAs alloys is

determined using inductively coupled plasma-optical emission spectrometry (ICP-OES), an accurate, elemental analysis technique proven to work well for AlGaAs.<sup>3</sup> At the same time, to the best of our knowledge, this technique has not been applied to epitaxial layers of AlGaInAs before.

Vurgaftman *et al.*<sup>4</sup> have written an excellent review of methods for determining the bandgap of compound semiconductors, including those of strained alloy compositions. Additionally, the work of Van de Walle on Model Solid Theory<sup>5</sup> is often referred to for the equations he shows to employ deformation potentials, originally introduced by Bardeen and Shockley,<sup>6</sup> for obtaining corrected bandgap values of a strained composition. We follow the notation found in Chuang, which is adapted from the Bir-Pikus Hamiltonian for strained semiconductors.<sup>7</sup> To determine the bandgap of any arbitrary alloy composition, initially, the “unstrained bandgap” is calculated, which reflects only the relation between the alloy's chemical composition and its bandgap but does not account for how that is affected by lattice strain (caused by lattice mismatch between the epitaxial layer and the host substrate). We note that the unstrained bandgap is not the same as the lattice-matched bandgap, for which

21 March 2024 08:53:03

TABLE I. Coefficients used for Olego's formulas [Eqs. (1) and (2)].

| Parameter  | P <sub>1</sub> | P <sub>2</sub> | P <sub>3</sub> | P <sub>4</sub> | P <sub>5</sub> | P <sub>6</sub> | P <sub>7</sub> |
|------------|----------------|----------------|----------------|----------------|----------------|----------------|----------------|
| Value (eV) | 0.36           | 2.093          | 0.629          | 0.577          | 0.436          | 1.013          | -2             |

one-dimensional interpolation equations have been published in the literature, which we do not evaluate herein. Strain on the lattice deforms the electronic band structure of the material and this effect can be calculated using tabulated deformation potentials.<sup>4</sup> This calculated strain effect on the bandgap is then added to the unstrained bandgap,<sup>8</sup> as demonstrated below.

There are three popular ways to find the unstrained bandgap ( $E_{gu}$ ). Two schemes are devised by Olego *et al.*, and one is based on the weighted sum of bandgaps of the constituent binaries.<sup>9-11</sup> In this paper,  $x$  and  $y$  correspond to Al and Ga atomic fractions, respectively, with  $z = 1 - x - y$ . Note that to calculate the bandgap for any composition (including ones that guarantee the presence of strain) the unstrained bandgap must be calculated.

The first scheme by Olego *et al.* (in the remainder of this paper, referred to as Olego I) is shown in Eq. (1). It was obtained by superposition of three empirical models coming from fits to data from three ternary compounds,<sup>10</sup>

$$E_{gu}[\text{eV}] = P_1 + P_2x + P_3y + P_4x^2 + P_5y^2 + P_6xy. \quad (1)$$

The second model of Olego *et al.* (in the remainder of this paper, referred to as Olego II) adds a fitted  $xyz$  term to account for bowing of the  $E_{gu}$  surface and is shown in Eq. (2),<sup>9</sup>

$$E_{gu}[\text{eV}] = P_1 + P_2x + P_3y + P_4x^2 + P_5y^2 + P_6xy + P_7xyz. \quad (2)$$

The parameters used for both Olego's models are shown in Table I.

The third scheme, weighted sum calculation, is based on the bandgaps of AlAs, GaAs, and InAs, as described below.

Boundary coordinates of the parameter space are calculated using Eq. (3),

$$u = \frac{1 - x + y}{2}, \quad (3a)$$

$$v = \frac{1 - y + z}{2}, \quad (3b)$$

TABLE II. Coefficients used for strained bandgap calculation, recommended in Ref. 4.

| Binary | Deformation potentials (eV) |                |      | Elastic stiffness constants (GPa) |                 | Lattice constant (Å) | Bandgap (eV)   | Varshni's coefficients |       |
|--------|-----------------------------|----------------|------|-----------------------------------|-----------------|----------------------|----------------|------------------------|-------|
|        | a <sub>c</sub>              | a <sub>v</sub> | b    | C <sub>11</sub>                   | C <sub>12</sub> | a                    | E <sub>g</sub> | α (meV/K)              | β (K) |
| AlAs   | -5.64                       | 2.47           | -2.3 | 1250                              | 534             | 5.6611               | 3.099          | 0.885                  | 530   |
| GaAs   | -7.17                       | 1.16           | -2   | 1221                              | 566             | 5.65325              | 1.519          | 0.5405                 | 204   |
| InAs   | -5.08                       | 1              | -1.8 | 832.9                             | 452.6           | 6.0583               | 0.417          | 0.276                  | 93    |

$$w = \frac{1 - x + z}{2}, \quad (3c)$$

with ternary bandgaps calculated with Eq. (4),

$$T_{\text{AlGaAs}} = u \times E_{g,\text{GaAs}} + (1 - u) \times E_{g,\text{AlAs}} + C_{\text{AlGaAs}} \times u \times (1 - u), \quad (4a)$$

$$T_{\text{GaInAs}} = v \times E_{g,\text{InAs}} + (1 - v) \times E_{g,\text{GaAs}} + C_{\text{GaInAs}} \times v \times (1 - v), \quad (4b)$$

$$T_{\text{AllnAs}} = w \times E_{g,\text{InAs}} + (1 - w) \times E_{g,\text{AlAs}} + C_{\text{AllnAs}} \times w \times (1 - w), \quad (4c)$$

with the quaternary unstrained bandgap expressed as in Eq. (5),

$$E_{gu}[\text{eV}] = \frac{x \times y \times T_{\text{AlGaAs}} + y \times z \times T_{\text{GaInAs}} + x \times z \times T_{\text{AllnAs}}}{x \times y + y \times z + x \times z}. \quad (5)$$

The ternary bowing parameters, used for the weighted sum model in the remainder of this study, are the following:<sup>4</sup>  $C_{\text{AlGaAs}} = -0.127 + 1.310x$ ,  $C_{\text{GaInAs}} = 0.477$ , and  $C_{\text{AllnAs}} = 0.7$

In the following explanations, all properties of the quaternary alloy are obtained by linear interpolation between the properties of its binary constituents shown in Table II. Note that binary bandgaps are given at 0 K, so Varshni's law has to be used to adapt those values to the 300 K temperature at which all measurements were carried out.

After calculating the bandgap for the unstrained lattice using one of the above-described approaches, the effect of strain on the bandgap is calculated using tabulated deformation potentials. The strain can be either calculated or derived from XRD measurement. The strain of the alloy deposited on the InP substrate is calculated as shown in Eq. (6), with  $\epsilon_{xx,yy}$  being the strain in the lattice plane and  $a$  being the lattice constant. Afterward, the strain in the out-of-interface-plane direction is calculated [Eq. (7)],

$$\epsilon_{xx} = \epsilon_{yy} = \epsilon = \frac{a_{\text{InP}} - a_{\text{AlGaInAs}}}{a_{\text{AlGaInAs}}}, \quad (6)$$

21 March 2024 08:53:03

$$\varepsilon_{zz} = -2 \frac{C_{12}}{C_{11}} \varepsilon. \quad (7)$$

Now, the strain-induced shifts of the conduction band ( $\delta E_c$ ), the heavy-hole band ( $\delta E_{hh}$ ), and the light-hole band ( $\delta E_{lh}$ ) can be calculated,

$$\delta E_c = a_c(\varepsilon_{xx} + \varepsilon_{yy} + \varepsilon_{zz}), \quad (8)$$

$$\delta E_{hh} = -P_\varepsilon - Q_\varepsilon, \quad (9)$$

$$\delta E_{lh} = -P_\varepsilon + Q_\varepsilon, \quad (10)$$

where

$$P_\varepsilon = -a_v(\varepsilon_{xx} + \varepsilon_{yy} + \varepsilon_{zz}), \quad (11)$$

$$Q_\varepsilon = -\frac{b}{2}(\varepsilon_{xx} + \varepsilon_{yy} - 2\varepsilon_{zz}). \quad (12)$$

The strained bandgap can be ultimately expressed as follows:

$$E_g [\text{eV}] = \begin{cases} E_{gu} + \delta E_c - \delta E_{hh} & \text{for } \varepsilon < 0, \\ E_{gu} + \delta E_c - \delta E_{lh} & \text{for } \varepsilon \geq 0. \end{cases} \quad (13)$$

Despite their importance in calculating strained bandgap energies, the review by Vurgaftman *et al.* emphasizes the large scatter in reported values of the deformation potentials.<sup>4</sup> Those large uncertainties, exacerbated by a multitude of used parameters, make the theoretical composition–bandgap relation less reliable. Furthermore, all methods of unstrained bandgap determination are, in fact, only interpolation schemes that do not encompass the complex physical reality of the relation between chemical composition and the bandgap. Both problems compel us to test the performance of several models using strained bandgap correction on a collection of almost 50 samples with  $\varepsilon$  ranging from  $-0.0105$  to  $+0.0023$ .

In an effort to fit multiple parameters to the experimental data, the differential evolution fitting algorithm as implemented in the Python package “LMFIT” is used.<sup>12</sup> This global optimization routine allows to avoid the risk of sub-optimal fitting caused by a local optimum. On the other hand, one must take into account that the differential evolution fitting algorithm is not perfect. The default parameters from LMFIT’s plug-and-play implementation are used, and it is known that differential evolution’s internal parameters are highly problem-dependent, and failure to adjust them can deliver not global, but local optimum.<sup>13</sup> Fine-tuning the algorithm’s internal parameters is, however, outside the scope of this paper and authors’ expertise, but independently, we performed a test of several fitting algorithms, confirming the superiority of the differential evolution algorithm in this case.

## II. EXPERIMENT

Samples were prepared by growing alloys of AlGaInAs between InP layers on 3 in. diameter InP wafers, using an Aixtron AIX2000 G2 planetary multi-wafer MOVPE reactor. As group III

precursors, metalorganics trimethylindium (TMI), trimethylaluminum (TMAl), and trimethylgallium (TMGa) were used, while group V elements were introduced as hydrides (arsine and phosphine). Typical growth conditions for the low-vacuum growth on InP substrates were used, with growth temperatures around 600° centigrade. The settings of the MOVPE reactor are used to determine the compositions of all the samples. The elemental flux into the MOVPE reactor of a metalorganic precursor depends on the carrier gas flowing through the bubbler source and the vapor pressure of the precursor inside the thermostated bubbler. For example, for hydrogen flowing through a bubbler containing TMGa, the TMGa flux into the reactor can be determined using Eq. (14),

$$\varphi(\text{TMGa}) = \frac{Q_{\text{H}_2} \times P_{\text{vapor, TMGa}}}{P_{\text{bubbler}} - P_{\text{vapor, TMGa}}}, \quad (14)$$

where  $Q_{\text{H}_2}$  is the hydrogen flow through the TMGa bubbler,  $P_{\text{vapor, TMGa}}$  is the TMGa vapor pressure, and  $P_{\text{bubbler}}$  is the bubbler’s pressure.<sup>14</sup> An identical formula can be applied for indium and aluminum (however, in the case of aluminum, the result must be multiplied by a factor of 2, because TMAl is present in the vapor phase as a dimer). The actual elemental composition of the deposited material can be determined by normalizing the precursor flux of each element to the total flux of these three precursors.

While using precursor flux proportions in order to determine the composition is an established method,<sup>14</sup> it is also known that reactor-based models do not account for local phenomena and the changes occurring within a reactor over time.<sup>15</sup> Verification of the established bandgap models and coefficients should not be carried out without, at least, basic validation of the obtained compositional data. Therefore, ICP-OES is used as a reference method to ensure acceptable precision of the presented results. The high accuracy of ICP-OES analysis (down to a relative 1% of molar ratio in proper conditions<sup>16</sup>) allows for an exact and direct determination of molar ratios in a solution, and has already proven to be a reliable technique for the analysis of III-V semiconductor epitaxial layers.<sup>3</sup> Unlike indirect methods, ICP-OES results are not affected by temperature, doping concentrations, or strain.<sup>3,17</sup> The low detection limit of ICP-OES (down to sub-ppb in some cases) allows it to accurately discern the relative elemental composition of an AlGaInAs layer of several tenths of micrometers thick grown on a 3 in. diameter InP wafer after it has been dissolved in a 100 ml of etchant solution, as is the case in this study.<sup>18</sup>

To validate the flux-based method of composition determination, the quaternary alloy is dissolved by using a piranha etchant that etches AlGaInAs approximately two orders of magnitude faster than the underlying InP material. Then, samples of the etch bath containing the dissolved In, Al, Ga, As, and P ions were submitted for analysis of ionic concentrations using ICP-OES. Due to the finite selectivity of the used etchant, while dissolving the quaternary epitaxial layers, some amount of the underlying InP substrate also dissolved. Therefore, to accurately determine the indium concentration in the grown layer, we measured the concentration of phosphorus in the solution to account for indium from the InP substrate (assuming a 1:1 ratio of dissolved In and P).

The bandgap of the alloy in each sample was determined from photoluminescence (PL) measurements at room temperature, mapped across a wafer. We have used the relationship between the bandgap and PL peak emission energy of  $E_{PL} = E_g + \frac{kT}{2}$ , with  $T = 300\text{K}$ .<sup>19</sup> It is known that the PL spectrum of certain AlGaInAs compositions on InP can show two peaks. While one peak is a result of the conventional band-to-band electronic transition, the second one comes from electrons recombining in a “trap” caused by band bending at the interface of the alloy and InP.<sup>20,21</sup> It was assured that the AlGaInAs bandgap is inferred only from band-to-band PL peaks. To avoid the PL blueshift caused by the quantum confinement effect, only layers with a thickness above 75 nm were included in this study.

Bandgap energies were obtained from PL by averaging the spectral position of the peak intensity for all measurements, within a 25 mm radius from each wafer’s center. The largest standard deviation of the peak position within such a region was 5.8 nm, and the average was 1.8 nm.

Because benchmarking of composition–bandgap models is limited by the accuracy of fabrication and measurements, the reproducibility of the experimental results needs to be studied. To do that, the data of depositions repeatedly realized with the same settings were collected and the standard deviations of the PL measurements were calculated for each group of settings. These data are shown in Table III.

The variability of these samples is shown in Fig. 1. Before the pooled standard deviation formula can be applied, it needs to be verified that the data are normally distributed. Therefore, knowing that it is robust against bimodal distributions, the Shapiro–Wilk normality test is used, yielding  $p = 0.52$ . This means that the data can, indeed, be considered normally distributed.

Because of the distribution’s normality, the data from Table III can be used to calculate the pooled standard deviation using Eq. (15),

$$\sigma = \sqrt{\frac{\sum_i (n_i - 1)\sigma_i^2}{\sum_i (n_i - 1)}}, \quad (15)$$

where  $n_i$  is the size of a population’s subset,  $\sigma_i$  is the subset’s standard deviation, and  $i$  numerates the subset. This calculation yields a pooled standard deviation of 6.6 nm, meaning that the

TABLE III. Data used to determine the wafer–wafer reproducibility within the dataset.

| Al (x) | Ga (y) | Quantity of such samples ( $n_i$ ) | Average PL wavelength (nm) | Sample–sample standard deviation ( $\sigma_i$ ) (nm) |
|--------|--------|------------------------------------|----------------------------|--|
| 0.036  | 0.399  | 6                                  | 1526                       | 2.9  |
| 0.142  | 0.297  | 5                                  | 1281                       | 10.4   |
| 0.145  | 0.302  | 4                                  | 1268                       | 6.8  |
| 0.220  | 0.202  | 2                                  | 1147                       | 0.7  |
| 0.238  | 0.204  | 4                                  | 1098                       | 5.2  |

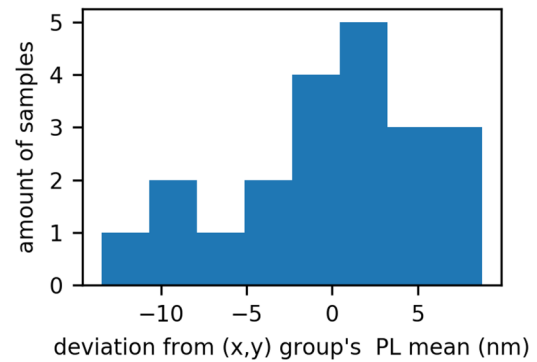


FIG. 1. Histogram of samples described in Table III, proven to be normally distributed.

reproducibility between different depositions is almost as good as the homogeneity within a single wafer. Such reproducibility allows for the use of the same weight for each data point in the fitting procedures.

In this article, several unstrained bandgap models that describe the relation between the chemical composition of AlGaInAs and its bandgap are benchmarked. To get insight into the performance of the existing models, residuals are defined as

$$r = \lambda_{\text{measured}} - \lambda_{\text{modeled}}. \quad (16)$$

The best model should have the smallest maximum residual, and in case of similar results, models can be compared by their median absolute residual, which should also be as small as possible. For the benchmarking process, it is assumed that the model can be considered accurate for  $\max(|r|) < 20\text{nm}$ .

### III. RESULTS AND DISCUSSION

#### A. Determination of AlGaInAs composition by ICP-OES

Table IV shows the compositions derived proportionally from the ICP-OES results along with the values obtained from the MOVPE reactor settings. The corresponding data are shown in Fig. 2, revealing a near 1:1 relation. To better assess the accuracy of using growth settings as input for the final alloy composition, a linear regression between the two sets of results is performed and the prediction intervals are calculated. Within the five sample dataset, the largest 95% prediction intervals were  $\pm 0.01$  for Al,  $\pm 0.016$  for Ga, and  $\pm 0.05$  for In. Only Al and Ga fractions were used as inputs in bandgap calculations. The small relative magnitudes of the inaccuracies make the MOVPE-based method to be considered satisfactory for the purpose of this study. The fitting data were not weighted for those inaccuracies, due to their small relative magnitude and the large number of samples investigated.

21 March 2024 08:53:03

TABLE IV. Experimental data used to validate the method of compositional analysis.

| Concentrations measured with ICP-OES |             |             |             | Elemental fractions calculated from ICP-OES and MOVPE settings |            |            |          |          |          |            |            |            |          |          |          |
|--------------------------------------|-------------|-------------|-------------|--|------------|------------|----------|----------|----------|------------|------------|------------|----------|----------|----------|
| Al (mmol/L)                          | As (mmol/L) | Ga (mmol/L) | In (mmol/L) | Al ICP-OES   | Ga ICP-OES | In ICP-OES | Al MOVPE | Ga MOVPE | In MOVPE | Al ICP-OES | Ga ICP-OES | In ICP-OES | Al MOVPE | Ga MOVPE | In MOVPE |
| 0.0281                               | 0.1245      | 0.0220      | 0.0953      | 0.234  | 0.183      | 0.582      | 0.22     | 0.202    | 0.578    | 0.582      | 0.183      | 0.582      | 0.22     | 0.202    | 0.578    |
| 0.0365                               | 0.1332      | 0.0307      | 0.0745      | 0.271  | 0.228      | 0.501      | 0.258    | 0.24     | 0.503    | 0.501      | 0.228      | 0.501      | 0.258    | 0.24     | 0.503    |
| 0.0245                               | 0.1688      | 0.0470      | 0.0922      | 0.155  | 0.298      | 0.547      | 0.145    | 0.302    | 0.553    | 0.547      | 0.298      | 0.547      | 0.145    | 0.302    | 0.553    |
| 0.0041                               | 0.0807      | 0.0297      | 0.0476      | 0.054  | 0.389      | 0.557      | 0.033    | 0.387    | 0.58     | 0.557      | 0.389      | 0.557      | 0.033    | 0.387    | 0.58     |
| 0.0055                               | 0.0920      | 0.0415      | 0.0535      | 0.059  | 0.446      | 0.495      | 0.04     | 0.447    | 0.513    | 0.495      | 0.446      | 0.495      | 0.04     | 0.447    | 0.513    |

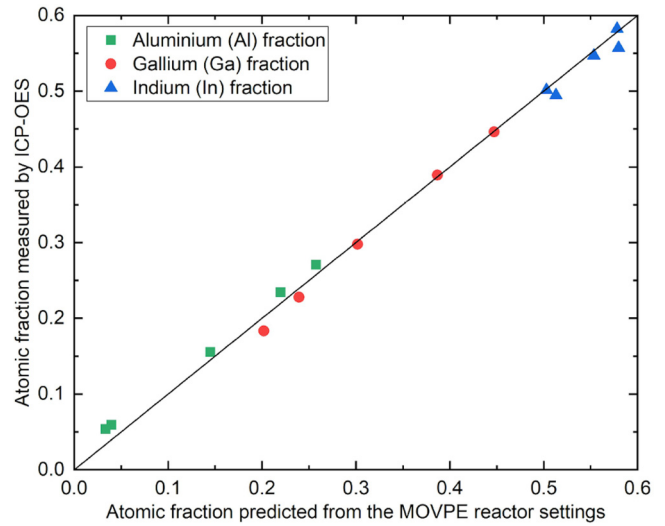


FIG. 2. Discrepancy between ICP-OES results, and the composition derived from the MOVPE reactor settings.

B. XRD investigation of the samples

To assure the sample quality, all samples were subjected to HRXRD scans using a Malvern-Panalytical X'Pert Pro MRD diffractometer. By matching the measured diffractograms to their simulations, we determined the lattice mismatch of the layers and confirmed the absence of relaxation. The strain calculated from XRD spectra is presented in Fig. 3 along with theoretical calculations based on interpolation between binary lattice constants. There is a visible offset; however, independent calculations revealed that there is no major difference between bandgap results obtained using one or the other strain metric. The bandgaps calculated in

21 March 2024, 08:53:03

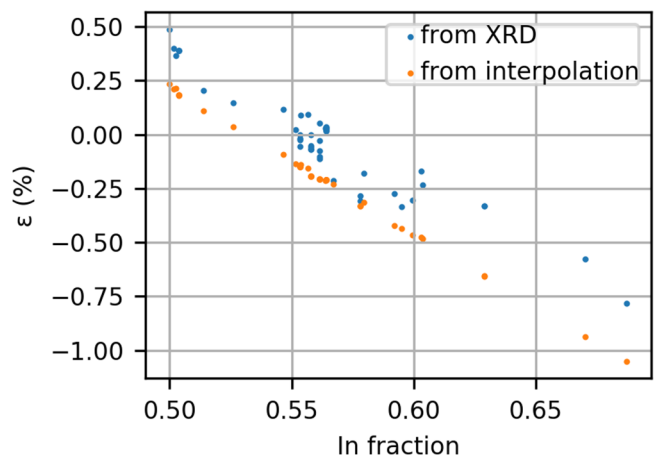


FIG. 3. Strain as a function of indium content for the samples under study, comparing the values calculated from Vegard's law to those measured by XRD.

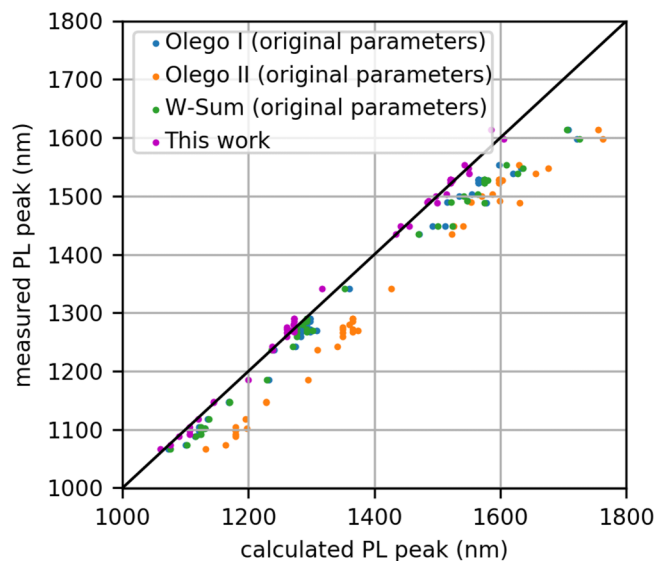


FIG. 4. Comparison of the proposed model with existing literature approaches.

Secs. III C–III E are performed using the interpolation-based strain as input. Particularly, when we do the statistical analysis of the PL residuals, as discussed below, excluding those samples that have the largest difference between the measured and calculated lattice mismatch from the analysis, we still end up with maximum residual values close to 100 nm, while the median residual value does not change meaningfully. Therefore, since both the maximum and median residual values are still not as low as we would like to see, we cannot conclude that the sample quality is the main factor in causing a large deviation between the calculated and measured PL or the bandgap value.

### C. Benchmark of interpolation schemes from the literature

The performance of the existing procedure using different unstrained bandgap models is compared with the experimental data. Figure 4 shows the performance of the three models introduced in Sec. I, as well as a fourth empirical model, which we describe in Sec. III F. While all models clearly follow the expected trends, the deviations of each model can be studied quantitatively when the residuals (as defined in Sec. II) are compared. Table V shows how accurately the models match the experimental data in terms of the median and maximum absolute residual values. As can be seen, with absolute residual median values between 30 and 81 nm, these

TABLE V. Residual statistics of the investigated models.

| Model        | Median $ r $ (nm) | Max $ r $ (nm) |
|--------------|-------------------|----------------|
| Olego I      | 30                | 123            |
| Olego II     | 81                | 164            |
| Weighted sum | 31                | 127            |

models are poor at predicting the outcome of a growth run, given the elemental composition. The Olego I model performs better than the other two models; however, the maximum absolute residual of 123 nm means this model is likely to give inaccurate predictions with particularly large residuals at high In content. These high residual values could be caused by both uncertainty in the value of the deformation potentials and the coefficients used in the unstrained bandgap equations. While there is a large spread of the reported values of deformation potentials,  $E_{gu}$  formula coefficients were derived from low-strain or binary samples (which correspond to a very limited compositional range).<sup>4,9,10</sup> Those limitations are generally known; however, using a large dataset (see the [supplementary material](#)), an attempt is made to pinpoint the main sources of large discrepancies between theory and experiment.

To understand the source of inaccuracies, the residual magnitude as a function of composition is analyzed, using the data shown in Fig. 5. The bandgap is mostly calculated by the addition of element-specific coefficients multiplied by their respective atomic fractions. This means that errors of the said coefficients will contribute to the result proportionally to relevant atomic fractions. In turn, when coefficients pertaining to one element are precise, an increase in the said element's amount will increase the precision of the result, causing the residual to approach zero. On the other hand, when coefficients pertaining to another element are imprecise, an increase in the element will cause the residuals to diverge from zero. This is a direct result of error propagation, with stoichiometric constraint of  $z = 1 - x - y$ , and with every variable ranging from 0 to 1. In preparation for Sec. III D, it is investigated which of the binaries (AlAs, GaAs, or InAs) contribute the least to the model's imperfection. This way, it can be determined which parameters shall be fitted, and which parameters can be kept as in the literature. Otherwise, any attempt at numerical fitting would be hampered by the parameter-to-sample ratio being too large.

There are three element-based observations that result from Fig. 5:

- The Al fraction relatively strongly correlates with absolute residuals decreasing for two of the  $E_{gu}$  formulas. It means that the AlAs parameters (Olego's coefficients, binary bandgaps, bowing coefficients, deformation potentials, etc.) are, in general, well-determined.
- The Ga fraction slightly contributes to the increase in  $|r|$  for two models.
- The In fraction relatively strongly correlates with residual worsening, no matter which  $E_{gu}$  formula is used in the strained bandgap calculation.

The above observations imply that more investigation of GaAs and InAs influence is needed to improve the applicability of all models.

### D. Fitting the deformation potentials

In the literature, there is a large scatter in the values of deformation potentials.<sup>4</sup> It is already mentioned in Sec. III C that the parameters related to AlAs seem to be very accurate. Therefore, it has been decided to perform the fit of GaAs and InAs deformation potentials to see if they are to blame for the inaccuracies. The

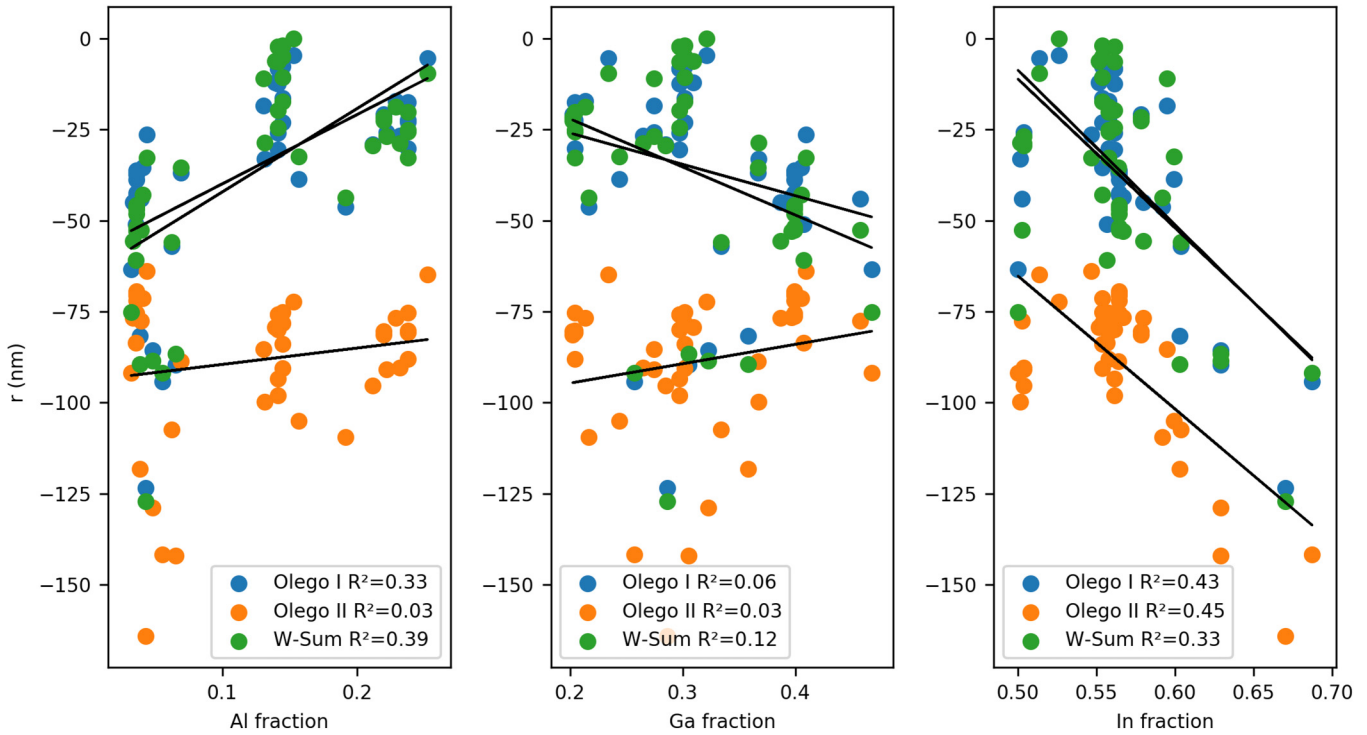


FIG. 5. Residuals of the investigated models as a function of the element and its atomic fraction, along with the coefficient of determination  $R^2$ .

boundaries (shown in Table VI) for each parameter correspond to the range reported in the literature (with the  $a_v$  sign-adjusted to commonly used convention).<sup>4</sup> Results of the fitting can be seen in Table VII, and the residual plots are shown in Fig. 6.

It seems that, in general, the Al fraction does not have a strong impact on the residuals, once more attesting to a good determination of AlAs parameters. It is also clear that fitting the In-related parameters strongly improved the impact of the In fraction on the residuals. Table VII presents the results of the deformation potentials' fits. Fitting them (especially with  $E_{gu}$  calculated with the Olego II formula) often yields one of the set boundary values. Obviously, searching within wider limits would likely lead to better results; however, that would not necessarily be physically meaningful. Because the calculated bandgap is a sum of the strain contribution and the unstrained contribution, the extreme values of the deformation potentials are probably used to compensate for the inaccuracies resulting from the imperfect unstrained bandgap formula.

Improvement in residuals is noticeable for all  $E_{gu}$  calculation methods; however, maximum  $|r|$  being well above 80 nm in each case suggests that one should seek the sources of inaccuracy within the  $E_{gu}$  calculation method, instead of deformation potentials.

### E. Fitting the coefficients of the unstrained bandgap formulas

It was shown in Sec. III D that fitting of the deformation potentials yields significant, yet unsatisfactory improvement to the models' residuals. Extreme values of the potentials, especially in the case of the Olego II method, suggest that much of the inaccuracy of the whole bandgap calculation procedure comes from the unstrained formula. It would be convenient to fit both deformation potentials and the unstrained formulas simultaneously. However, these attempts yielded poor results, which can be attributed to the

TABLE VI. Parameter space for the fits of the deformation potentials used in this section.

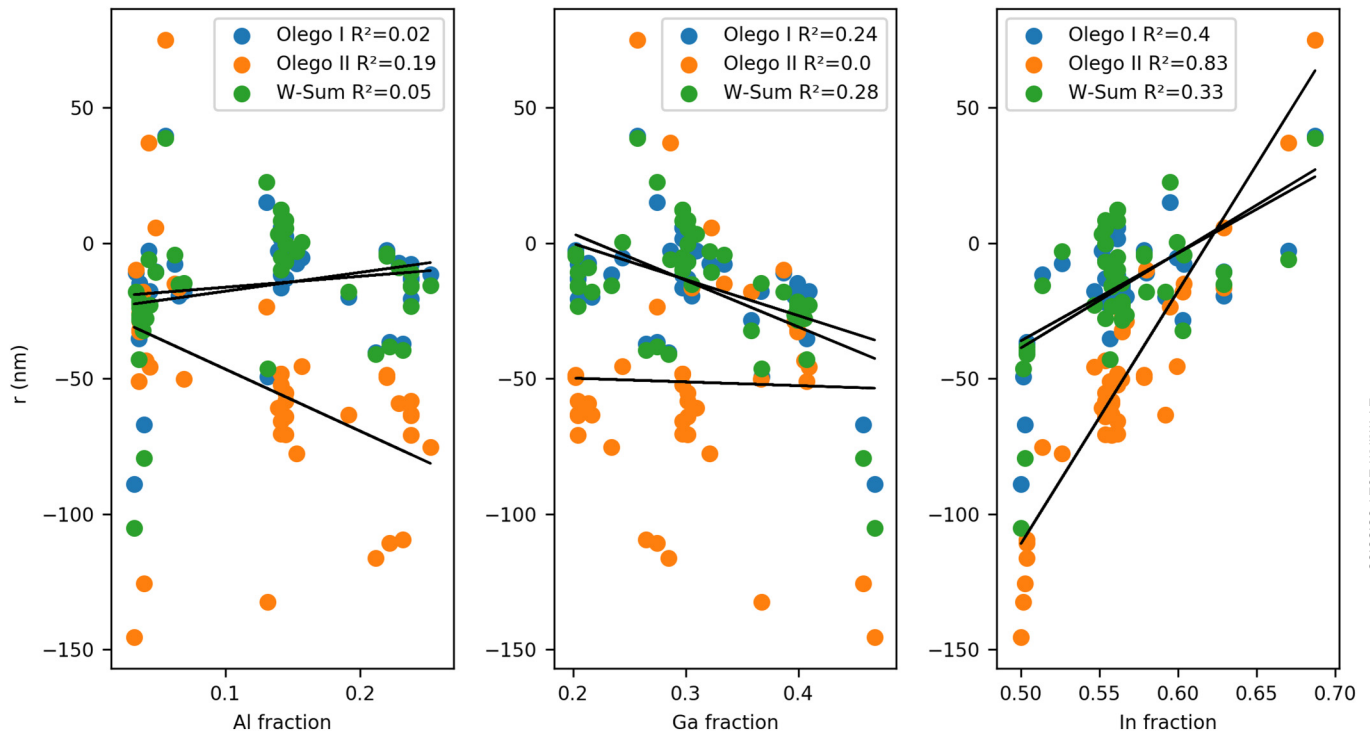
|             | GaAs       |            |        | InAs       |            |        |
|-------------|------------|------------|--------|------------|------------|--------|
|             | $a_c$ (eV) | $a_v$ (eV) | b (eV) | $a_c$ (eV) | $a_v$ (eV) | b (eV) |
| Upper limit | -6.3       | 2.1        | -1.66  | -5.08      | 5.2        | -2.57  |
| Lower limit | -18.3      | 0.2        | -3.9   | -11.7      | 1.0        | -8.0   |

21 March 2024 08:53:03



**TABLE VII.** Results of the deformation potentials optimization. L and U signify the result being equal to the parameter's lower and upper boundary, respectively. Numbers in parentheses correspond to the metric's change compared to Table V.

|              | GaAs       |            |          | InAs       |            |          | Median $ r $ (nm) | Max $ r $ (nm) |
|--------------|------------|------------|----------|------------|------------|----------|-------------------|----------------|
|              | $a_c$ (eV) | $a_v$ (eV) | $b$ (eV) | $a_c$ (eV) | $a_v$ (eV) | $b$ (eV) |                   |                |
| Olego I      | -8.79      | 0.65       | -1.66 U  | -11.70 L   | 3.98       | -2.57 U  | 15 (-15)          | 89 (-34)       |
| Olego II     | -18.30 l   | 2.10 U     | -1.66 U  | -11.70 L   | 5.20 U     | -2.57 U  | 52 (-29)          | 146 (-18)      |
| Weighted sum | -11.09     | 2.00       | -1.66 U  | -11.33     | 2.80       | -2.57 U  | 16 (-15)          | 105 (-22)      |



21 March 2024 08:53:03

**FIG. 6.** Residuals of the investigated models as a function of element and its atomic fraction, along with the coefficient of determination  $R^2$ , after optimizing the deformation potentials only.

**TABLE VIII.** Optimized coefficients for  $E_{gu}$  models, according to formulas 1, 2, and 4. L and U signify the result being equal to the parameter's lower and upper boundary, respectively.

|                     | $P_1$ (eV)              | $P_2$ (eV)              | $P_3$ (eV)              | $P_4$ (eV)              | $P_5$ (eV)              | $P_6$ (eV) | $P_7$ (eV) |
|---------------------|-------------------------|-------------------------|-------------------------|-------------------------|-------------------------|------------|------------|
| Olego I             | 0.414 U                 | 1.991                   | 0.600                   | 0.664 U                 | 0.371 L                 | 0.861 L    | N/A        |
| Olego II            | 0.414 U                 | 2.241                   | 0.616                   | 0.490 L                 | 0.371 L                 | 0.861 L    | 1.7 L      |
| <i>Weighted sum</i> |                         |                         |                         |                         |                         |            |            |
| $E_g(\text{AlAs})$  | $E_g(\text{GaAs})$ (eV) | $E_g(\text{InAs})$ (eV) | $C(\text{AlGaAs})$ (eV) | $C(\text{GaInAs})$ (eV) | $C(\text{AlInAs})$ (eV) |            |            |
| 3.068               | 1.51 L                  | 0.45 U                  | 1.183 U                 | 0.348                   | 0.240                   |            |            |

**TABLE IX.** Residual statistics of the investigated models, after optimization of the unstrained bandgap formulas. Numbers in parentheses correspond to the metric's change compared to Table V.

| Model        | Median $ r $ (nm) | Max $ r $ (nm) |
|--------------|-------------------|----------------|
| Olego I      | 12 (-18)          | 45 (-78)       |
| Olego II     | 11 (-70)          | 43 (-121)      |
| Weighted sum | 12 (-19)          | 50 (-77)       |

number of fitted parameters becoming too large compared to the size of the dataset.

To test the hypothesis that the model's inaccuracy stems from the inaccuracy of the unstrained bandgap formula, the coefficients of the unstrained bandgap formulas [see Eqs. (1), (2), and (5)] are fitted while setting the deformation potentials to the values recommended in the literature (see Table II).

The boundaries for fitting Olego I and Olego II formulas were  $\pm 15\%$  of the original ones described in Sec. I. Parameter boundaries for the weighted sum model were the same as the ranges reported in Vurgaftman's review. The resulting coefficients are shown in Table VIII. Not that many of the parameters are at the boundaries of the searched parameter space.

The results of applying the fitted parameters are displayed in Table IX. The resulting improvement is dramatic, confirming that

the unstrained bandgap formulas are, indeed, the main source of inaccuracy.

Figure 7 displays residuals as a function of the atomic fraction of each element. In the case of all  $E_{\text{gu}}$  models, the Al and Ga fractions do not affect the residual strongly. The residual slightly varies with the indium fraction, once more suggesting that the impact of indium on the quaternary alloy's properties requires further research. Since the maximum absolute residual is still unsatisfactory for all models, a novel model is proposed in Sec. III F.

## F. Empirical model of AlGaInAs-on-InP bandgap

As shown in Secs. III C to III E, finding the optimal parameters of the existing method is a very difficult task. The improvement offered by fitting known parameters to the experimental data is not satisfactory from a practical point of view. Since growing strained AlGaInAs of a properly defined bandgap is of paramount value to the industry and academia, in this section, a simplistic model to calculate the strained bandgap as a function of the alloy's composition is proposed, based on fitting to the dataset [see Eq. (17)]. In this model, six parameters are utilized, so it reflects band dynamics differences under compressive and tensile conditions (explained in detail in Ref.7) while keeping the simplicity that enables a good fit. This model encompasses the "unstrained alloy" component along with the electronic effects introduced by the strain. Deriving the model using the data from strained samples makes it unique since

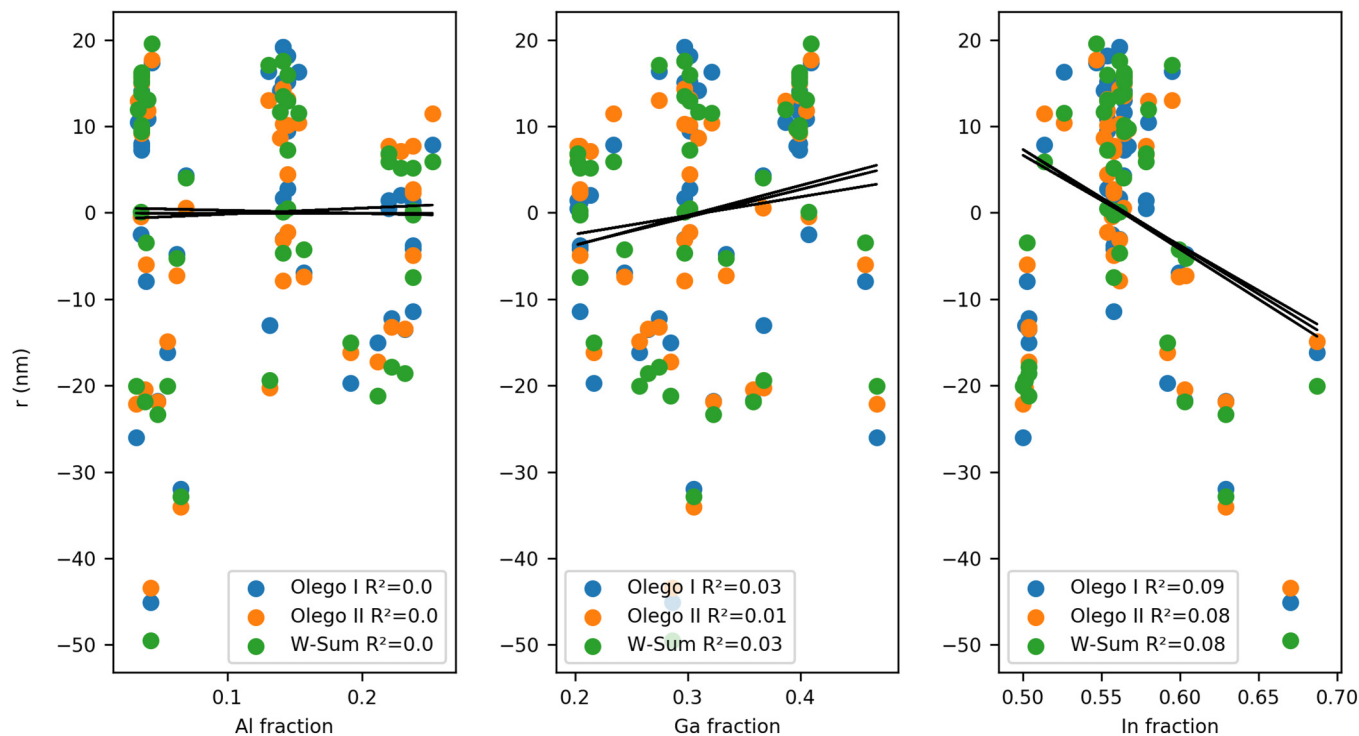


**FIG. 7.** Residuals of the investigated models as a function of element and its atomic fraction, along with the coefficient of determination  $R^2$ , after optimizing the unstrained formulas only.

21 March 2024 08:53:03

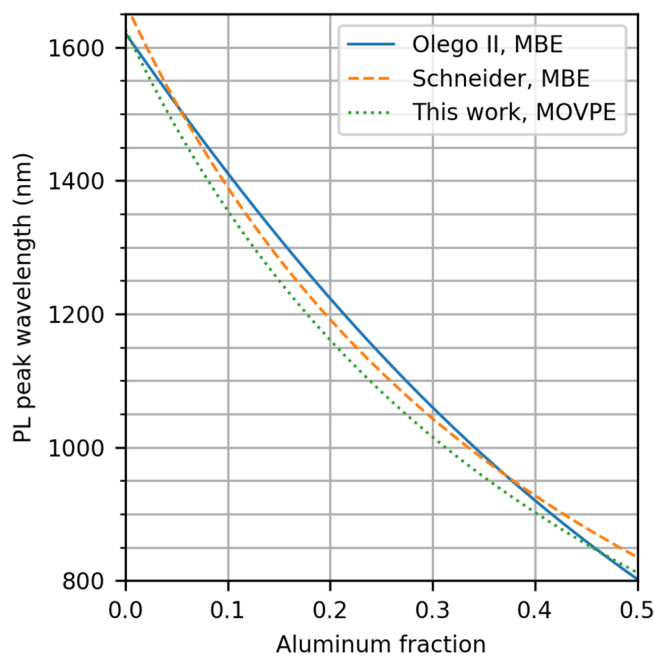


FIG. 8. Comparison of three models (room temperature, lattice-matched).

most of the literature is based on the lattice-matched alloy.

$$E_g = \begin{cases} 2.53(\pm 0.02)x + 1.03(\pm 0.02)y + 0.53(\pm 0.01)z & \text{for } \varepsilon < 0, \\ 3.00(\pm 0.00)x + 1.47(\pm 0.03)y + 0.11(\pm 0.02)z & \text{for } \varepsilon \geq 0. \end{cases} \quad (17)$$

The performance of this novel model is summarized in Table X.

The standard deviation of all residuals is just 0.4 nm smaller than the wafer-wafer reproducibility reported in Sec. II.  $R^2$  between each atomic fraction and residuals is 0.03, 0.01, and 0.02 for Al, Ga, and In, respectively, indicating that the new model is not biased against any composition. This model is, to our best knowledge, the most accurate in the available literature.

Substituting variables of Eq. (17) using the lattice-matching condition, i.e.,  $x + y \cong 0.47$ ,<sup>10</sup> it can be algebraically shown that both cases of the equation are nearly identical, with differences on the second decimal place. This inaccuracy can be attributed to most of the samples having negative  $\varepsilon$  and could be improved by investigating more samples. Interestingly, such lattice-matched solution of the model often results in lower PL peak wavelengths than those

TABLE X. Residual statistics of the proposed empirical model.

| Model         | Median $ r $<br>(nm) | Max $ r $<br>(nm) | $\sigma(r)$<br>(nm) | Average $ r $<br>(nm) |
|---------------|----------------------|-------------------|---------------------|-----------------------|
| Empirical fit | 6.08                 | 29.00             | 6.20                | 7.35                  |

calculated with Olego's and Schneider's fits,<sup>9,22</sup> as shown in Fig. 8. Since stoichiometries are the same for all calculations, and all models were obtained from precise data, it is assumed that the discrepancies originate from the growth condition or measurement differences and that influenced each team's model. A more thorough study should be carried out to find out the ultimate reason for such differences. This way, a model accounting for the alloy disorder in the bandgap calculation could be more widely used due to a better understanding of the phenomenon.<sup>23</sup> The authors of the said model also noted a large literature scatter of the reported bandgap values, and such a thorough study would probably address this issue.

#### IV. CONCLUSIONS

In this paper, a benchmark of three formulas for the unstrained bandgap of AlGaInAs in conjunction with bandgap energy correction for strain is performed. It is demonstrated that commonly used parameters do not yield satisfying results for a strained alloy. Furthermore, it was shown that the largest contributor to inaccuracy is the unstrained bandgap term. We also found that more research is needed to understand GaAs and InAs effects on bandgap. This paper introduces a simple and empirical formula that accurately predicts the bandgap of AlGaInAs on InP substrates, accounting for the strain effects. However, this study is limited by three factors: the absence of optimization of the fitting algorithm itself, the majority of the samples being compressively strained, and that a proper fitting of all deformation parameters would require even more samples. In the future, it would be desirable to collect more data and test more sophisticated unstrained bandgap models proposed by others.<sup>23,24</sup> Furthermore, it would be interesting to further research the influence of AlGaInAs growth conditions on its stoichiometry-bandgap relation.

#### SUPPLEMENTARY MATERIAL

See the supplementary material for compositional, PL, and XRD data.

#### ACKNOWLEDGMENTS

The authors would like to acknowledge Bas van der Merbel for technical support, Peter Thijs for his mentoring, and Jeroen Lammers of eurofins Eindhoven for ICP OES analysis. This work was supported by the European Union's Horizon 2020 Research and Innovation Programme (Marie Skłodowska-Curie Grant No. 813467).

#### AUTHOR DECLARATIONS

##### Conflict of Interest

The authors have no conflicts to disclose.

#### Author Contributions

**Marcin Zyskowski:** Conceptualization (lead); Data curation (lead); Formal analysis (lead); Investigation (lead); Methodology (equal); Software (lead); Validation (lead); Visualization (lead); Writing – original draft (lead); Writing – review & editing (supporting).  
**Nick de Louw:** Conceptualization (supporting); Data curation

21 March 2024 08:53:03

(supporting); Formal analysis (supporting); Investigation (supporting); Software (supporting); Validation (supporting); Visualization (supporting); Writing – original draft (supporting). **Steven Kleijn:** Conceptualization (equal); Data curation (supporting); Formal analysis (equal); Funding acquisition (equal); Investigation (equal); Methodology (equal); Project administration (lead); Resources (equal); Software (supporting); Supervision (lead); Validation (lead); Visualization (equal); Writing – original draft (supporting); Writing – review & editing (leading). **Francisco Javier Díaz Otero:** Funding acquisition (lead); Project administration (lead); Resources (lead); Supervision (supporting); Writing – original draft (supporting).

## DATA AVAILABILITY

The data that support the findings of this study are available from SMART Photonics and from the authors upon reasonable request.

## REFERENCES

- <sup>1</sup>J. Decobert, N. Lagay, C. Cuisin, B. Dagens, B. Thedrez, and F. Laruelle, “MOVPE growth of AlGaInAs–InP highly tensile-strained MQWs for 1.3  $\mu\text{m}$  low-threshold lasers,” *J. Cryst. Growth* **272**(1–4), 543–548 (2004).
- <sup>2</sup>S. R. Semic, T.-M. Chou, J. Sih, J. B. Kirk, A. Mantie, J. K. Butler, D. Bour, and G. A. Evans, “Design and characterization of 1.3- $\mu\text{m}$  AlGaInAs–InP multiple-quantum-well lasers,” *IEEE J. Sel. Top. Quantum Electron.* **7**(2), 340 (2001).
- <sup>3</sup>K. A. Bertness, C. M. Wang, M. L. Salit, G. C. Turk, T. A. Butler, A. J. Paul, and L. H. Robins, “High-accuracy determination of epitaxial AlGaAs composition with inductively coupled plasma optical emission spectroscopy,” *J. Vac. Sci. Technol., B* **24**(2), 762 (2006).
- <sup>4</sup>I. Vurgaftman, J. R. Meyer, and L. R. Ram-Mohan, “Band parameters for III–V compound semiconductors and their alloys,” *J. Appl. Phys.* **89**(11), 5815–5875 (2001).
- <sup>5</sup>C. G. Van de Walle, “Band lineups and deformation potentials in the model-solid theory,” *Phys. Rev. B* **39**(3), 1871–1883 (1989).
- <sup>6</sup>J. Bardeen and W. Shockley, “Deformation potentials and mobilities in non-polar crystals,” *Phys. Rev.* **80**(1), 72–80 (1950).
- <sup>7</sup>S. L. Chuang, “Physics of Optoelectronic Devices” (John Wiley & Sons, 2009).
- <sup>8</sup>J. Minch, S. H. Park, T. Keating, and S. L. Chuang, “Theory and experiment of InGaAsP and InGaAlAs long-wavelength strained quantum-well lasers,” *IEEE J. Quantum Electron.* **35**(5), 771 (1999).
- <sup>9</sup>D. Olego, T. Chang, E. Silberg, E. Caridi, and A. Pinczuk, in *Inst. Phys. Conf. Ser. No. 65: Chapter 3. Paper presented at Int. Symp. GaAs and Related Compounds, Albuquerque* (1982), p. 195–202.
- <sup>10</sup>D. Olego, T. Y. Chang, E. Silberg, E. A. Caridi, and A. Pinczuk, “Compositional dependence of band-gap energy and conduction-band effective mass of  $\text{In}_{1-x-y}\text{Ga}_x\text{Al}_y\text{As}$  lattice matched to InP,” *Appl. Phys. Lett.* **41**(5), 476–478 (1982).
- <sup>11</sup>C. K. Williams, T. H. Glisson, J. R. Hauser, and M. A. Littlejohn, “Energy bandgap and lattice constant contours of III–V quaternary alloys of the form,” *J. Electronic Materials* **7**(5), 8 (1978).
- <sup>12</sup>M. Newville, T. Stensitzki, D. B. Allen, and A. Ingargiola (2014). “LMFIT: Non-linear least-square minimization and curve-fitting for Python” [Zenodo](#).
- <sup>13</sup>M. Leon, “Improving differential evolution with adaptive and local search methods,” Thesis (Mälardalen University, 2019).
- <sup>14</sup>M. A. Herman and H. Sitter, “Epitaxy physical principles and technical implementation,” in *Softcover Reprint of the Hardcover*, 1st ed. (Springer, Berlin, 2004).
- <sup>15</sup>M. Ebert, K. A. Bell, S. D. Yoo, K. Flock, and D. E. Aspnes, “*In situ* monitoring of MOVPE growth by combined spectroscopic ellipsometry and reflectance-difference spectroscopy,” *Thin Solid Films* **364**, 22–27 (2000).
- <sup>16</sup>C. Morrison, H. Sun, Y. Yao, R. A. Loomis, and W. E. Buhro, “Methods for the ICP-OES analysis of semiconductor materials,” *Chem. Mater.* **32**(5), 1760–1768 (2020).
- <sup>17</sup>K. Bertness, T. Harvey, A. Paul, L. Robins, G. Turk, T. Butler, and M. Salit, in *North American Conference on Molecular Beam Epitaxy (NAMBE 2003)*, Keystone, CO, USA (2003).
- <sup>18</sup>G. Tyler, “ICP-OES, ICP-MS and AAS Techniques Compared” (Jobin Yvon of Horiba Group, 1995).
- <sup>19</sup>E. F. Schubert, *Light-Emitting Diodes* (Cambridge University Press, 2003).
- <sup>20</sup>O. J. Pitts, W. Benyon, and A. J. SpringThorpe, “Modeling and process control of MOCVD growth of InAlGaAs MQW structures on InP,” *J. Cryst. Growth* **393**, 81–84 (2014).
- <sup>21</sup>M. Sacilotti, F. Motisuke, L. Horiuchi, R. Landers, L. Cardoso, and B. Waidman, “Growth and characterization of type-II/type-I AlGaInAs/InP interlaces,” *J. Crystal Growth* **124**, 589–595 (1992).
- <sup>22</sup>J. M. Schneider, J.-T. Pietralla, and H. Heinecke, “Control of chemical composition and band gap energy in  $\text{Ga}_x\text{In}_{1-x-y}\text{Al}_y\text{As}$  on InP during molecular beam epitaxy,” *J. Cryst. Growth* **175–176**, 184–190 (1997).
- <sup>23</sup>Y. S. Yong, H. Y. Wong, H. K. Yow, and M. Sorel, “A convenient band-gap interpolation technique and an improved band line-up model for InGaAlAs on InP,” *Appl. Phys. B* **99**(3), 477–486 (2010).
- <sup>24</sup>T. Mei, “Interpolation of quaternary III–V alloy parameters with surface bowing estimations,” *J. Appl. Phys.* **101**(1), 013520 (2007).